ACS Photonics

pubs.acs.org/journal/apchd5 Article

Defocus-Insensitive Microscopy via Spatial Phase Modulation Using End-to-End Learning

Panu Hildén,* Sebastian Kalt, Markus Nyman, Sami Hamriti, Martin Wegener, Carsten Rockstuhl, and Andriy Shevchenko

Cite This: https://doi.org/10.1021/acsphotonics.6c01233 Read Online

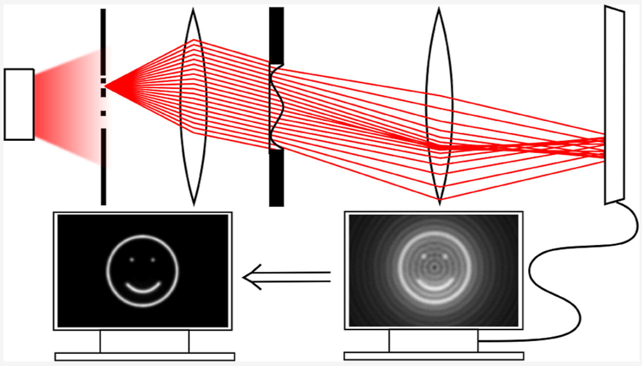

ABSTRACT: In optical microscopy, high spatial resolution comes at the cost of a short depth of field. This trade-off prevents the formation of sharp images of three-dimensional objects or objects moving in and out of focus. Moreover, it is often difficult to know the extent to which the object is out of focus, which makes it challenging to determine the point spread function that describes the blurring. This hinders the ability to restore the blurred image using digital postprocessing. To resolve these issues, we design a phase mask that, when inserted into the microscope, extends the depth of field, making the point spread function insensitive to the location of the object. We leverage end-to-end machine learning tools to design this phase mask together with a Richardson-Lucy-type deconvolution algorithm to remove image blurring. The phase mask is then manufactured with a commercial 3D nanoprinter and used in a microscope to demonstrate defocus-insensitive imaging of microfabricated objects. The experiments successfully verify the operation of both the phase mask and the image restoration algorithm.

KEYWORDS: *optical microscopy, depth of field, phase mask, end-to-end learning, image restoration, 3D laser nanoprinting*

INTRODUCTION

Digital postprocessing can be used to restore images degraded by blurring and noise inherent to optical imaging systems. Traditionally, this has been accomplished using deconvolution-based techniques,[1,2] whereas neural networks trained to process images has gained popularity in recent years.[3−5] The learning capabilities of neural networks can also be combined with the physical interpretability of deconvolution processes within physics-informed neural networks.[6−8] Regardless of the chosen method, image restoration becomes substantially more challenging when the object to be imaged or a part of it is considerably out of focus. First, the defocus broadens the point spread function (PSF), blurring the image. This suppresses the high-frequency content of the image, as described by the optical transfer function (OTF), making the restoration process more susceptible to noise.[9−12] Second, the exact shape of the PSF tends to vary significantly as a function of the focusing error, especially in high-resolution systems, such as microscopes. Not only does this make it difficult to know the PSF required for nonblind deconvolution, the blurring varies between parts of an image of a three-dimensional object. This behavior prevents the use of blind deconvolution algorithms that assume the PSF to be shift-invariant throughout the recorded image.[13,14] Problems of this type can be remedied by engineering the PSF of the system, utilizing amplitude masks[15−18] or phase masks,[9,19−26] the latter of which have the added benefit of being completely lossless. Other methods, such as ghost imaging[27−30] and single-pixel imaging[31,32] can also be used to obtain sharp images in the presence of severe aberrations, but they are usually slow and based on relatively complex optical setups. Imaging systems whose PSF vary slowly as a function of defocus can be realized using a standalone phase mask,[19,20,22] combining a mask with a lens,[21,25,33−35] or by placing a mask in the Fourier plane of a 4*f*-imaging system.[18,26,36,37] However, the slow size variation of the PSF is often accompanied by its shape variation, making image restoration difficult. While radially asymmetric phase masks can be used to generate modulation transfer functions (MTF) nearly independent of defocus,[11,23,33,38] the phase of the resulting OTF varies significantly, introducing artifacts in the restored images.[39,40] In contrast, a circularly symmetric

Received: May 19, 2026
Revised: August 24, 2026
Accepted: August 27, 2026

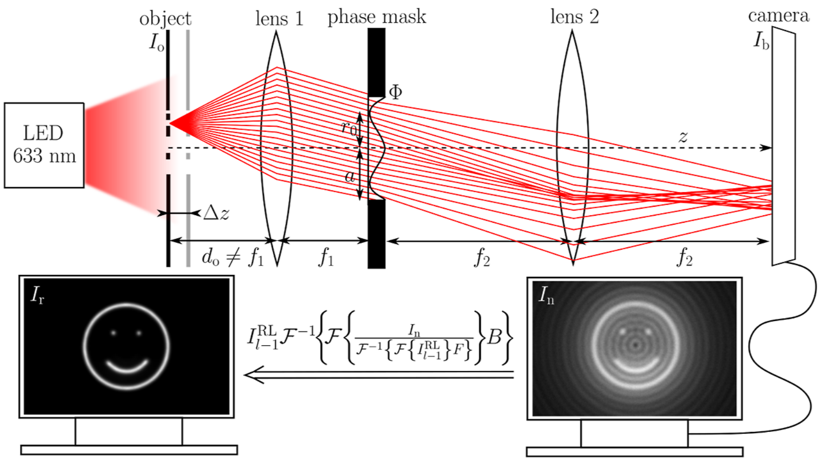

Figure 1. A 4f imaging system with a phase mask to be optimized. Light transmitted by the object, having the intensity profile I_o, forms a blurred image with intensity I_b on the detector array of the camera. The intensity signal recorded by the camera, I_n, is further degraded by shot noise. The Richardson-Lucy deconvolution algorithm is then applied to the recorded image, resulting in the restored image with intensity I_r. The radial profile of the phase mask contains a single stationary point at a distance r_0 from the optical axis, while varying rapidly everywhere else. This results in a PSF resembling a Bessel beam, as indicated by the rays propagating at the same angle with respect to the z-axis at the output.

phase mask yields a real-valued OTF, removing the phase-modulation problem.[41] For this reason, we aim to design a circularly symmetric phase mask, here, to be used in a defocus-insensitive microscope.

In general, the longitudinal variance of the OTF can be reduced at a cost of impairing its response to high-frequency content of the object to be imaged.[10,42] Many of the phase mask designs set limit to the minimum value of OTF within a targeted spatial-frequency range to avoid excessive noise amplification during the restoration process, which then limits the longitudinal invariance of the frequency response.[10,11] However, it is often unclear whether the quality of the restored images is degraded more by poor high-frequency response or by non-negligible longitudinal variation of the OTF. Here, in order to maximize the depth of field of the microscope while still accounting for the noise, we circumvent this problem by simulating the image degradation and subsequent restoration for a set of training images and optimize the phase mask profile based on the quality of the processed images. This strategy is well-aligned with the end-to-end design paradigm, in which the imaging system and the restoration algorithm are jointly optimized. While the approach is a natural choice for optimizing systems that employ neural networks,[37,43,44] it has also been used for systems utilizing deconvolution algorithms.[45−48]

The phase masks designed to improve image restoration typically assume that the image degradation is dominated by additive readout noise, in which case images can be restored using a Wiener filter.[11,45,49,50] Here, in contrast, we are concerned with shot noise. Images blurred by a known PSF and degraded by shot noise can be restored using the Richardson-Lucy deconvolution.[51,52] However, the iterative nature of the algorithm makes it relatively slow. This problem was recently addressed by introducing a Wiener-Butterworth back projector, which significantly reduces the number of iterations required to restore the image.[53] The back projector, however, depends on multiple parameters that need to be optimized.[7,53]

In this work, we present a defocus-insensitive microscope in the form of a 4f imaging system, the Fourier plane of which contains a circularly symmetric phase mask designed to enable deconvolution-based image restoration. To the best of our knowledge, such microscopes were not introduced before. The illuminating light is assumed to be spatially incoherent, as in the majority of optical microscopes. The imaged objects can be located at an unknown distance from the focal plane, be spatially extended along the optical axis, or move through the focal plane with no influence on the image quality due to the large depth of field of the system. The phase mask profile is optimized in tandem with the Richardson-Lucy algorithm accelerated by the Wiener-Butterworth back projector. The optimization is performed using a machine-learning style algorithm implemented within Tensorflow (Python). The designed phase mask is manufactured using a 3D nanoprinter, and its performance is verified experimentally along with the image restoration algorithm.

■ RESULTS AND DISCUSSION

Defocus-Insensitive Microscope

In this section, we explain the operation principle of the microscope we propose, supporting the explanations by simple analytical derivations. The microscope is constructed in the form of a 4f imaging system, shown schematically in Figure 1. The first lens is a microscope objective and the second one is a tube lens. The object is shown as a thin transparency illuminated by spatially incoherent light, e.g., from an LED. The transparency can be shifted by a distance $\Delta z = f_1 - d_0$ from the front focal plane of the system. In the common focal plane of the two lenses, we introduce a phase mask filling a circular aperture of radius a. The detector array of the camera is located in the back focal plane of the second lens. The phase mask is made of glass with radially varying thickness, and the goal is to optimize its profile such that the PSF becomes independent of Δz. The system is assumed to be shift-invariant so that the intensity distribution in the image plane can be modeled by the following convolution[54]

$$I_b(x, y, \Delta z) = h(x, y, \Delta z) * I_g(x, y) \tag{1}$$

where $h(x, y, \Delta z)$ is the defocus-dependent intensity PSF of the system and $I_g(x, y) = I_o(x/M, y/M)$ is the intensity of the perfectly sharp geometrical-optics image of the object,

https://doi.org/10.1021/acsphotonics.6c01233
ACS Photonics XXXX, XXX, XXX−XXX

magnified by factor $M = -f_2/f_1$ (including image inversion). Introducing normalized coordinates

$$v = \frac{k_0 \mathrm{NA}\sqrt{x^2 + y^2}}{|M|} \text{and} \tag{2}$$

$$u = \frac{k_0 \Delta z \mathrm{NA}^2}{2} \tag{3}$$

and using the Fresnel diffraction integral, the shape of the PSF is given by[18,55]

$$h(u, v) = |\int_0^1 \exp[\mathrm{i}(\Phi(\rho) + u\rho^2)]J_0(v\rho)\rho \mathrm{d}\rho|^2 \tag{4}$$

Here, $\Phi(\rho)$ is the radial phase-shift profile of the phase mask, $J_0(v\rho)$ is the zeroth-order Bessel function, $k_0 = 2\pi/\lambda_0$ is the wavenumber corresponding to the central wavelength of the illumination, $\rho = r/a$ is the normalized radial coordinate in the Fourier plane, and $\mathrm{NA} \approx a/f_1$ is the numerical aperture of the imaging system, which is determined by the radius of the phase mask a. The displacement Δz is defined such that, for $\Delta z > 0$, the object is closer to the imaging system, whereas for $\Delta z < 0$, it is farther away from the system. The normalized coordinate u can also be expressed in terms of the defocus coefficient as $u = k_0 W_{20}$.[23] The radial phase profile of the mask is written in the form of a polynomial

$$\Phi(\rho) = \sum_{n=1}^{N} p_n \rho^n \tag{5}$$

The coefficients p_n must be optimized to minimize the dependence of the PSF on the normalized defocus u, thus extending the depth of field.

For a microscope to be insensitive to defocus, the PSF should resemble a nondiverging Bessel beam, like in an imaging system utilizing a thin annular aperture.[18] To see how this can be achieved, consider a phase mask with a rapidly varying profile $\Phi(\rho)$ except for a single stationary point at $\rho = s_0$, where the phase gradient is zero. The total argument of the exponential function in eq 4 depends on the defocus and is given by

$$\Psi(\rho, u) = \Phi(\rho) + u\rho^2 \tag{6}$$

The defocus-dependent stationary point $\rho = s$ is found from

$$\Psi'(s, u) = \Phi'(s) + 2us = 0 \tag{7}$$

where the prime denotes the derivative with respect to ρ. For such a phase mask, eq 4 can be solved using the method of stationary phase (see ref 56) near the optical axis (where $J_0(v\rho)$ varies slowly as a function of ρ), yielding the following Bessel-like PSF

$$h(u, v) = \left|\exp\left(\mathrm{i}\left\{\Psi(s, u) + \mathrm{sign}[\Psi''(s, u)]\frac{\pi}{4}\right\}\right)\sqrt{\frac{2\pi}{|\Psi''(s, u)|}}sJ_0(sv) + \exp[\mathrm{i}\Psi(1, u)]\frac{J_0(v)}{\mathrm{i}\Psi'(1, u)}\right|^2 \tag{8}$$

where the two terms correspond to light transmission through the stationary point and light diffraction at the edge of the phase mask, respectively. The ray-optics picture of the formation of a Bessel-like beam is shown in Figure 1, where the (red) rays that cross the mask near the stationary points propagate at the same angle with respect to the z-axis after the second lens. Such rays result in a Bessel beam.[57] Famously, for a quartic phase mask, the on-axis intensity of the PSF, $h(u, 0) = 2\pi s^2/|\Psi''(s, u)|$ (neglecting the second term in eq 8), is independent of defocus.[9,21] Nevertheless, despite the Bessel-like shape, the width of this PSF varies as a function of defocus. The mainlobe of the PSF given by eq 8 has a normalized width $v_0(u) = 2.4048/s(u)$ that depends on the radial position of the stationary point $s(u)$ that varies as a function of defocus at a rate given by the expression

$$\begin{aligned} \frac{\partial \Psi'(s, u)}{\partial u} &= \Phi''(s)\frac{\partial s}{\partial u} + 2\left(s + u\frac{\partial s}{\partial u}\right) = 0 \\ \Rightarrow \frac{\partial s}{\partial u} &= \frac{-2s}{\Psi''(s, u)}. \end{aligned} \tag{9}$$

From eq 9, we see that the longitudinal variation of the PSF can be reduced by increasing $|\Psi''(s, u)|$, i.e., by making the phase mask's surface angle $\arctan(\Phi'(\rho)/[k_0(n - 1)a])$ vary rapidly near the stationary point. However, as $|\Psi''(s, u)|$ increases, the on-axis intensity decreases, signifying that more light gets refracted far away from the axis, where the method of stationary phase no longer applies. Due to this, there is an unavoidable trade-off between minimizing the longitudinal variation of the OTF and maximizing its response to large $k_r = \sqrt{k_x^2 + k_y^2}$ up to the diffraction limited cutoff frequency $k_{\mathrm{dl}} = 2\mathrm{NA}k_0$. A poor frequency response reduces contrast and makes the image restoration process more sensitive to noise. However, the inspection of the OTF alone does not clearly reveal which of the two mechanisms has a bigger impact on the final image. To avoid this problem, we adopt a machine-learning-inspired optimization strategy. The performance of the imaging system, including the image restoration, is simulated for a set of training images. The phase mask profile, alongside the deconvolution algorithm, is then optimized based on the quality of the simulation results, as described below.

Optimization Procedure

In our end-to-end learning-based optimization approach, the profile of the phase mask is represented by a polynomial function of normalized radial distance ρ given in eq 5. The polynomial coefficients are determined by improving the restored images of the training objects for prescribed values of Δz, as shown in Figure 1. To use the approach correctly, the relevant degradations of the training images need to be simulated. First, the images are blurred according to eqs 1 and 4. Then, the images are deteriorated further by noise. Here, we assume that the images are corrupted mainly by shot noise. Given a noise-free discretized blurred image, a pixel (n, m) of which takes the value $I_b[x_n, y_m]$ in the units of expected number of photons impinging on the pixel, the noisy image can be modeled by generating Poisson-distributed random variables $I_n[x_n, y_m] \sim \mathrm{Pois}(I_b[x_n, y_m])$. However, the randomly generated signals at each pixel are not differentiable with respect to I_b and by extension with respect to the polynomial coefficients of the phase mask profile. This fact would prevent the use of the gradient-based optimization. In order to bypass this problem and make I_n differentiable, we employ an approximate expression

$$I_n[x_n, y_m] = I_b[x_n, y_m] + \sqrt{I_b[x_n, y_m]}X_{nm} \tag{10}$$

https://doi.org/10.1021/acsphotonics.6c01233
ACS Photonics XXXX, XXX, XXX−XXX

where $X_{nm} \sim \mathcal{N}(0, 1)$ are normally distributed random variables with zero mean and unit variance. The expression accurately mimics the Poisson statistics at sufficiently large $I_b[x_n, y_m]$ (>10 photons),[58,59] and it can be differentiated as X_{nm} are independent of I_b, enabling the optimization.

After simulating the image degradation, the optimization procedure includes a postprocessing step for image restoration. An efficient method for restoring blurred images corrupted by shot noise is to use Richardson-Lucy deconvolution algorithm, the lth iteration of which is given by the expression

$$I_l^{\mathrm{RL}} = I_{l-1}^{\mathrm{RL}} \frac{I_n}{I_{l-1}^{\mathrm{RL}} * f} * b \tag{11}$$

where f and b are the forward and back projectors, respectively, usually chosen to be equal to the PSF.[53] Here, the exact PSF cannot be used, due to the lack of knowledge about the defocus. Instead, the Fourier transform of the forward projector is taken to be a weighted average of the OTFs

$$F = \sum_{m=1}^{M} w_m H(u_m, k_r) \tag{12}$$

where the longitudinal coordinates, u_m, are evenly distributed within the system's intended depth of field. The weights $w_m > 0$ ($\|\mathbf{w}\|_1 = 1$) are parameters to be optimized alongside the phase mask profile. To accelerate the convergence of the Richardson-Lucy deconvolution, we adopt the Wiener-Butterworth back projector recently proposed in ref 53. The Fourier transform of the back projector is a product of the Wiener and the Butterworth filters ($B = B^{\mathrm{W}}B^{\mathrm{B}}$) given by expressions

$$B^{\mathrm{W}} = \frac{F^*}{|F|^2 + \alpha} \tag{13}$$

$$B^{\mathrm{B}} = \left[1 + \epsilon^2\left(\frac{k_x^2 + k_y^2}{k_{\mathrm{dl}}^2}\right)^{\gamma}\right]^{-1/2} \tag{14}$$

respectively, where

$$\epsilon^2 = \frac{B^{\mathrm{W}}(k_{\mathrm{dl}})^2}{\beta^2} - 1 \tag{15}$$

The asterisk stands for complex conjugation. The parameters α, β, and γ are optimized as part of the end-to-end design. These parameters dictate the noise amplification or suppression, the appearance of ringing artifacts, and the convergence rate of the iterative algorithm. The convergence is accelerated by making the product $FB(k_r)$ flat over the range of spatial frequencies to be restored.[53] During the deconvolution, the spectral resolution of the images is increased by padding. This can introduce more artifacts, which we try to minimize using symmetric (reflective) padding.[60,61]

After the image degradation (due to blur and noise) and subsequent restoration have been simulated for a batch of training images, their quality is assessed to measure the performance of the imaging system and the restoration algorithm. Here, the quality of the restored images, represented by the intensity I_r at each pixel, is quantified by a loss function that combines the intensity L_1-norm error with the structural similarity index measure (SSIM[62])

$$\mathcal{L} = \frac{\|I_r - I_g\|_1/N + 1 - \mathrm{SSIM}(I_r, I_g)}{2} \tag{16}$$

where N is the number of pixel in each image. Such functions are found to perform well in image restoration tasks.[6,63] Like in ref 63, the two terms are equally weighted for simplicity. In eq 16, the images are normalized such that the brightest pixel takes the value of unity, hence $\mathcal{L} \in [0, 1]$.

The simulated imaging system is configured to match our experimental setup, which consists of an objective lens with focal length f_1 = 45 mm and a tube lens with f_2 = 200 mm, resulting in magnification $|M|$ = 4.4. The phase mask radius is a = 1 mm. The objects are illuminated with a 633 nm LED (Thorlabs M625L3), and the images are recorded using a Basler ace 2 a2A2448-75ucBAS camera with a 2448 × 2048 array of 2.74 μm wide pixels. The system is optimized for objects displaced by up to ±10 mm from the front focal plane. To this end, the training data (3200 images taken from ImageNet-Sketch data set[64]) is divided into batches of 64 images whose displacements from the front focal plane, Δz, are evenly distributed within the interval [-10 mm,10 mm], which corresponds to normalized defocus $u \in [-24.5, 24.5]$. As a preprocessing measure, the training data is scaled such that the geometric-optics images occupy a 1024 × 1024 pixel region at the center of the camera, corresponding to objects of size 631 × 631 μm^2. In addition, the training images are low-pass filtered with a Butterworth-filter with cutoff frequency $1.2k_{\mathrm{dl}}$, removing the features that cannot be restored even when the object is in focus. After simulating the blurring, the images are cropped and binned to a size of 1024 × 1024 pixels, which have an effective width of 2 × 2.74 μm/$|M|$ ≈ 1.2 μm. This accelerates the fast Fourier transforms (FFTs) performed during the deconvolution. The amount of noise in the images is characterized by the expected number of photons incident on the brightest (binned) pixel, which is set to 1000. The simulated level of noise is similar to what is seen in the experiments.

The number of iterations performed during deconvolution cannot be optimized, but must be fixed in advance. For the optimization, we use five iterations. This exceeds the typically required number when employing the Wiener-Butterworth back projector.[53] Using a slightly larger number of iterations reduces the need for the back projector to strongly amplify high spatial frequencies, to which the phase mask is expected to respond poorly, as discussed earlier. At the same time, the iteration count remains low enough to preserve the acceleration benefits of the modified back projector. The number of iterations can later be adjusted depending on the application.

Following the recommendations in the Supporting Information of ref 53, the deconvolution is initialized with parameters $\alpha = \beta = 10^{-3}$ and $\gamma = 10$. The forward projector is initially computed using equal weights $w_m = 1/64$. To obtain an initial Bessel-like PSF, we first evaluate the loss function in eq 16 for quartic phase masks of the form $\Phi = p_4\rho^4 - p_2\rho^2$, choosing polynomial coefficients p_2 and p_4 that minimize $\mathcal{L}$. The polynomial coefficients are constrained to yield modulation depths $(\Phi_{\max}-\Phi_{\min})/[k(n-1)] = p_2^2/[2p_4k(n-1)] \in [0, 15\,\mu\mathrm{m}]$ and stationary points $s_0 = \sqrt{p_2/(2p_4)} \in [0.5, 0.9]$. The chosen quartic phase mask is then used as a starting point for a gradient-descent optimization algorithm to find the coefficients for the 20-

https://doi.org/10.1021/acsphotonics.6c01233
ACS Photonics XXXX, XXX, XXX−XXX

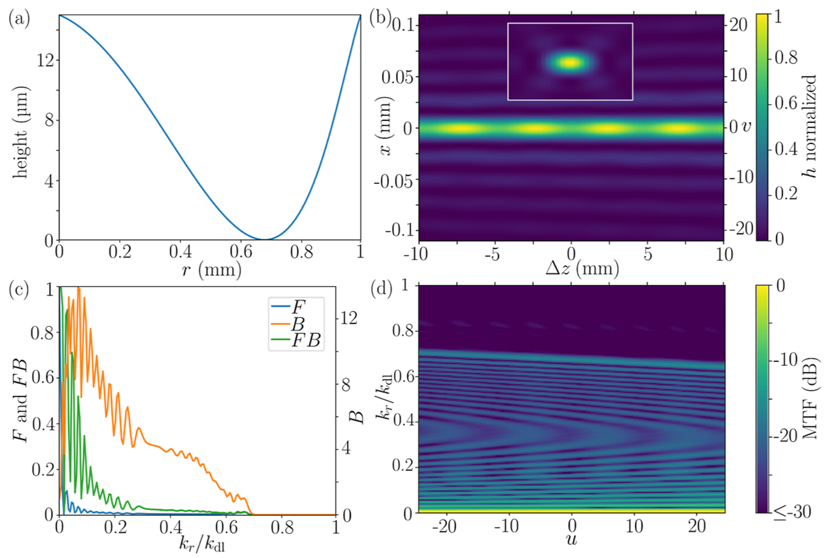

Figure 2. Results of the optimization. (a) The radial profile of the phase mask height, corresponding to the set of polynomial coefficients {−42.3, −238.6, 28.1, 272.8, −12.6, −10.6, −4.4, 1.6, 5.9, 8.2, 8.9, 8.3, 6.8, 4.6, 2.0, −1.0, −4.2, −7.6, −11.1, −14.6}. (b) The PSF as a function of displacement Δz (see also the corresponding coordinate u below) for the system including the phase mask. For comparison, the conventional PSF obtained in the absence of the phase mask is shown in the inset using the same scale. (c) The Fourier transforms of the forward and backward projectors, as well as their product. (d) The frequency response of the imaging system (MTF) on a logarithmic scale $10\ \log_{10}|H|$ dB, as a function of normalized coordinate u (see the corresponding displacement Δz above).

degree polynomial given by eq 5. The additional degrees of freedom compensate for the drawbacks of the quartic phase mask that become apparent when calculating the PSF numerically instead of using the method of stationary phase.[25] However, as the higher-order terms have only a minor contribution to the phase mask shape (similarly to the rational phase mask considered in ref 25), the degree of the polynomial can be limited to a small number. The optimization is implemented in Python using the TensorFlow package.[65] It employs the ADAM optimizer[66] with a learning rate of 10^{-1}, and is ran until the loss function stops converging. This took 111 epochs for the phase mask presented in this work. The modulation depth of the phase mask is limited to 15 μm to ensure the validity of eq 4. This gives us a rough shape of the phase mask, which is then optimized further, now alongside the parameters of the deconvolution process, i.e., $\mathbf{w}$, α, β, and γ, using the same algorithm as before, but with a lower learning rate of 10^{-4}. The joint optimization was complete after 74 epochs. Note that, in contrast to neural-network-based restoration methods, the deconvolution algorithm depends only on a couple of parameters, the optimization of which cannot overfit the training data. Hence, a separate validation data set is not required to assess generalization performance.[67]

The optimized phase mask profile and the corresponding PSF as a function of displacement Δz are shown in Figure 2a,b, respectively. The phase of the mask varies rapidly far from the sole stationary point $s_0 \approx 0.7$, forming a Bessel-like PSF, as predicted by the method of stationary phase. The Bessel-like PSF is nearly independent of defocus, unlike the PSF obtained without the phase mask shown in the inset of Figure 2b. That said, the on-axis intensity exhibits small sinusoidal variation, which can be attributed to the interference between the light passed through the stationary point and the light diffracted from the edge of the phase mask (the second term in eq 8). It is also worth noting that the main lobe of the Bessel-like PSF has approximately the same width as the Airy pattern obtained without the phase mask. This differs from a Bessel-like PSF generated by an annular aperture, where the main lobe is significantly narrower.[18] Here, a broader beam results from an effective numerical aperture that is determined by the stationary point rather than the full aperture radius, i.e., $\mathrm{NA}_{\mathrm{eff}}(u) = s(u)\mathrm{NA}$. Consequently, the OTF as well as the forward and backward projectors of the deconvolution algorithm have cutoff frequencies around $0.7k_{\mathrm{dl}}$ as shown in Figure 2c,d. The frequency response shown in Figure 2d indicates that the cutoff frequency, given by $k_{\mathrm{cutoff}}(u) = s(u)k_{\mathrm{dl}}$, varies almost linearly with Δz in the range [-10 mm,10 mm] with a slope given by eq 9. Figure 2d uses a logarithmic scale to highlight the cutoff frequency, whereas the forward projector in Figure 2c is shown on a linear scale to better illustrate the frequency response. Figure 2c also shows the curve of the product *FB*, which is not flat. This indicates that the optimized back projector sacrifices the convergence speed to prevent excessive amplification of high-frequency noise. Near the cutoff, *B* decreases gradually in order to avoid the formation of ringing artifacts. Despite the compromised speed, the backward projector offers significant acceleration compared to the conventional Richardson-Lucy algorithm, as demonstrated in the next section.

Experiments

To experimentally verify the performance of the optimized imaging system, the phase mask was manufactured using two-photon grayscale lithography (2GL) and a custom developed precompensation routine to correct for systematic deviations of the phase mask surface from the designed height profile introduced by the manufacturing process. The phase mask printing was performed with a Nanoscribe Quantum X system using the commercial photoresist IP-S (Nanoscribe GmbH & Co. KG) and a 25×/NA0.8 microscope objective lens (Zeiss, LD LCI Plan-Apochromat Imm Corr DIC M27). To achieve a good surface quality, the phase mask was printed using a slicing distance of 1 μm, a bidirectional hatching with a line distance of 0.2 μm, a scan speed of 20 cm/s, a dynamic laser power in

https://doi.org/10.1021/acsphotonics.6c01233
ACS Photonics XXXX, XXX, XXX−XXX

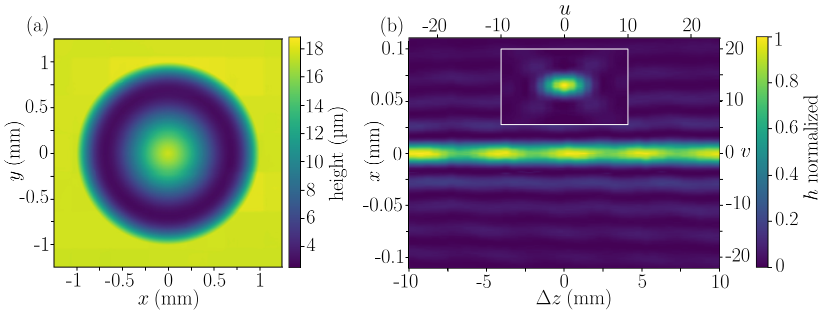

Figure 3. (a) The measured height profile of the fabricated phase mask. (b) The experimentally measured PSF for the imaging system containing the phase mask. The PSF measured without the phase mask is shown in the inset.

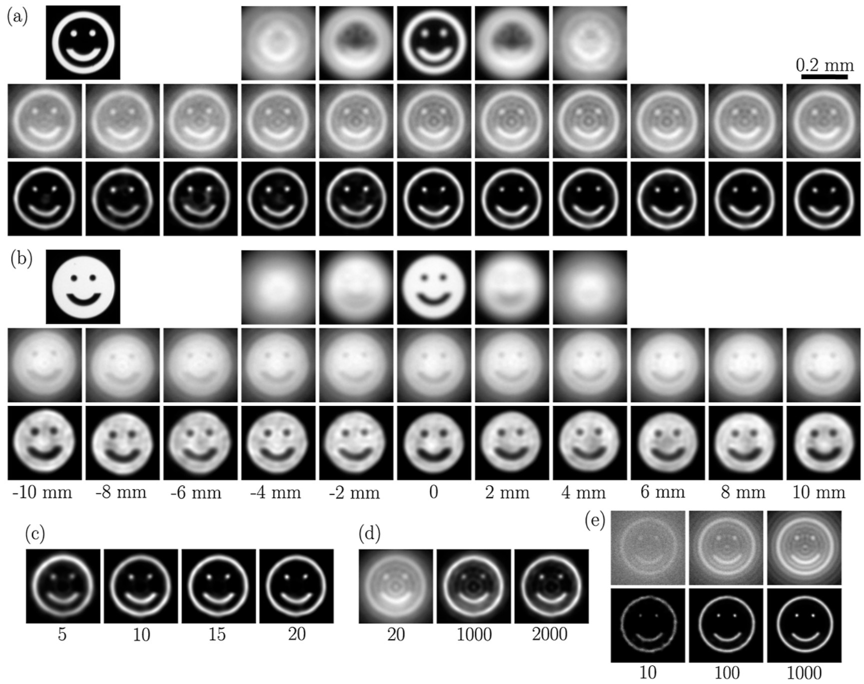

Figure 4. (a) Images of a smile icon (etched into an opaque aluminum film) displaced from the front focal plane by a distance $\Delta z \in$ [-10 mm,10 mm], as indicated below. Top row contains images taken without the phase mask, as well as an additional high resolution image (on the left). The two rows below show the images obtained with the phase mask, before and after applying the deconvolution (with 15 iterations). (b) Images of a different smile icon. (c) The restored in-focus images after 5, 10, 15, and 20 iterations with the optimized Wiener-Butterworth backward projector. (d) The restored images after 20, 1000, and 2000 iterations with the conventional backward projector. (e) Simulated images of smile corrupted by shot noise with 10, 100, and 1000 photons on the brightest pixel (top row), as well as the corresponding image restored by the deconvolution algorithm (bottom row).

the range between 8 mW and 50 mW, and 2GL print field stitching. The obtained surface quality of the phase mask was analyzed with a reflection-based spinning-disk confocal microscope (MarSurf CM explorer S/W, Mahr GmbH). After two iterations of precompensating print artifacts (see refs 26 and 67), we obtained an average absolute difference of μ_{abs} = 118.9 nm between the fabricated phase mask and the designed height profile with a standard deviation of σ = 190.1 nm. Hence, this technique yields high surface quality with deviations much smaller than the wavelength of light. The fabricated phase mask, the measured height profile of which is shown in Figure 3a, is inserted into the microscope (setup shown in Figure 1 and described in the above section) and the performance of the system is studied.

We start by measuring the PSF of the system. The transverse profiles of the PSFs are obtained by taking images of a pinhole with a 5 μm diameter illuminated from behind. To characterize the PSF as a function of defocus, the pinhole was mounted on a translation stage and displaced along the optical axis in 0.5 mm increments, with the images recorded at each position. The resulting PSF of the system containing the phase mask is shown in Figure 3b, while the inset displays the PSF measured in the absence of the phase mask. The agreement between the theoretical and experimental PSFs (see the insets in Figures 2b and 3b, respectively) confirms that the performance of the system is limited by diffraction rather than aberrations (excluding defocus). With the phase mask in place, the measured PSF exhibits the expected Bessel-like structure, confirming the extended depth of field. Compared to the theoretical prediction, the sinusoidal intensity variation along the optical axis appears to be shifted. This discrepancy can be attributed to a phase shift between the two interfering contributions in eq 8, e.g., if the aperture radius deviates from its nominal value. However, the sinusoidal modulation

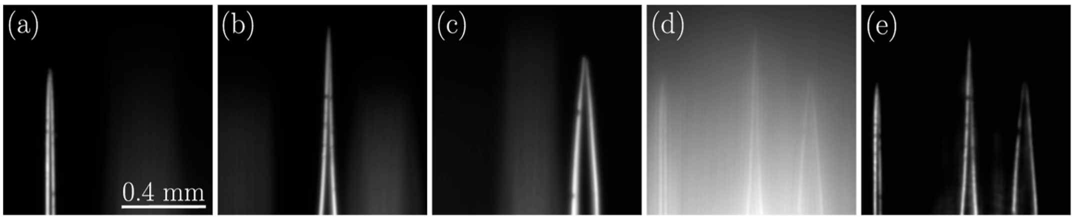

Figure 5. Images of three tapered optical fibers placed 9 mm apart along the optical axis of the system. The first three images are taken in the absence of the phase mask, such that (a) the proximal, (b) the central, and (c) the distal fiber is placed in the focal plane of the objective. The last two images are taken with the phase mask inserted in the setup (d) before and (e) after applying the deconvolution. In these two images, the central fiber is located in the focal plane.

averages out when calculating the forward projector, and therefore, its influence on the image quality is expected to be negligible. It is also worth noting that, while the Bessel-like nature of the PSF is shown only for the 633 nm wavelength, it holds over the whole visible spectral range, which was observed by us experimentally and can also be seen from eq 8 and the values of the refractive index and extinction coefficient of the phase-mask's material reported in ref 68.

The performance of the system is demonstrated using a microfabricated test object in the form of a 'smile' pattern etched into a thin aluminum film on top of a glass plate. The sample is mounted on a translation stage, allowing the images to be recorded at its various displacements from the front focal plane. The results are presented in Figure 4a together with a high-resolution image of the object (on the left). The top row shows the images acquired without the phase mask. The images in the middle row are obtained with the phase mask present in the setup, but prior to deconvolution, while the bottom row shows the corresponding images restored by the deconvolution algorithm. Figure 4b presents the same sequence of images for a second test sample, which is the negative of the first one. In the absence of the phase mask, the images become unrecognizable when the sample is slightly shifted from the focal plane. In contrast, the phase mask renders the images insensitive to defocusing, as intended. This enables restoration of the images using the deconvolution algorithm. The quality of the deconvolved images is comparable to the in-focus images in the absence of the phase mask, indicating that the algorithm is able to restore the level of detail available in the spatial frequency band $k_r \leq k_{\mathrm{cutoff}}$. However, the relatively low NA of the imaging system leads to some differences in the images compared to the high-resolution ones, in particular, in the width of the lines forming the 'smile'. Here, after about 15 iterations, the quality of the deconvolved images stopped improving. This can be seen from Figure 4c, which shows the restoration of the in-focus image for various iteration numbers. In each iteration, most of the time is taken by the two FFTs and inverse FFTs of 2048 × 2048 padded image. On a run of the mill computer (here HP EliteBook 840 with Intel Core i5-1335U), they take around 10 ms each, indicating that real-time imaging is easy to achieve. While the ability of the back projector to accelerate the deconvolution is compromised, it still speeds up the restoration process significantly compared to the traditional Richardson-Lucy deconvolution. This is demonstrated in Figure 4d that depicts the same image, but deconvolved using the forward projector also as a back projector. The figure shows that the method requires around 2000 iterations to reach similar image quality as the optimized back projector.

The experiments demonstrate the performance of the imaging system for a noise level typical for a microscope. However, the restoration algorithm also works well even in low-light conditions with much more noise. Figure 4e proves this with simulated images of a smile icon under different levels of shot noise. The images before and after deconvolution are shown in the top and bottom rows, respectively. The restored image quality stays high even when the expected number of photons on the brightest pixel drops to 100. Only when the photon number falls to an extremely low value, such as 10, does the image quality deteriorate.

To demonstrate the ability of the system to simultaneously image multiple objects at various axial positions, we place three tapered optical fibers approximately 9 mm apart from each other along the optical axis. In the horizontal direction, the three fibers cover 80% of the detector area and thereby rely on the shift-invariance of the PSF for the deconvolution to work. The fibers are illuminated from two sides using the 633 nm LED and a white-light source (LEICA CLS 160X). Figure 5a−c shows the images acquired without the phase mask such that (a) the proximal, (b) the central, and (c) the distal fiber is brought to focus by shifting the object. While the in-focus fiber forms a sharp image, the other two fibers are significantly blurred and hard to discern. However, when the phase mask is inserted in the setup, all three fibers can be seen simultaneously, as shown in Figure 5d. In this case, the central fiber is located in the focal plane. Then, applying the deconvolution algorithm, we obtain equally sharp images of all the fibers simultaneously, as shown in Figure 5e.

■ CONCLUSIONS

We have employed an end-to-end optimization approach to jointly design a phase mask and optimize a Richardson-Lucy deconvolution algorithm for restoring sharp images of objects located at unknown distances from the front focal plane of a microscope. The microscope is a 4*f* imaging system with the phase mask positioned in the Fourier plane. The phase mask profile was designed to produce a Bessel-beam-like PSF by simulating the performance of the system for a set of training images, so that the loss of image quality due to severe defocus and poor high-frequency response of the OTF could be balanced. The images, degraded also by shot noise, were restored using a Richardson-Lucy deconvolution algorithm accelerated by a Wiener-Butterworth back projector, the free parameters of which were optimized in tandem with the phase mask. The designed phase mask was fabricated using two-photon grayscale lithography with a nanoscale precision. The PSF was measured to show good agreement with the theory. The phase mask and the deconvolution algorithm were experimentally demonstrated to provide sharp images of

https://doi.org/10.1021/acsphotonics.6c01233
ACS Photonics XXXX, XXX, XXX−XXX

microfabricated objects displaced by up to ±10 mm from the front focal plane of the system, as designed. The setup is also shown to work well when simultaneously imaging multiple objects located at different distances from the objective. This finding demonstrates that the presented method is a practical approach for developing defocus-insensitive optical microscopes.

The quality of the images formed by the system could be improved by increasing its NA, e.g., by using an objective lens with a shorter focal length. While this would reduce the depth of field (see eq 3), its increase relative to the system without the phase mask would stay the same. Note also that the depth of field demonstrated in this work is much longer than most of the practical microscope observations would require. Although we optimized the phase mask jointly with a deconvolution algorithm, the same end-to-end framework could be extended to train a neural network for image restoration. One could also try to exploit the defocus-dependent cutoff frequency of the system for estimating the longitudinal positions of the objects. For most objects, the cutoff frequency can be identified from the Fourier transform of the recorded image, enabling estimation of the displacement Δz. This positional information is valuable in its own right and would also allow selection of the exact PSF required for exact deconvolution.

AUTHOR INFORMATION

Corresponding Author

Panu Hildén − *Department of Applied Physics, Aalto University, Aalto FI-00076, Finland;* orcid.org/0000-0002-1167-062X; Email: panu.hilden@aalto.fi

Authors

Sebastian Kalt − *Institute of Applied Physics, Karlsruhe Institute of Technology, Karlsruhe 76131, Germany;* orcid.org/0009-0004-8848-8991

Markus Nyman − *Institute of Nanotechnology, Karlsruhe Institute of Technology, Karlsruhe 76131, Germany*

Sami Hamriti − *Institut d'Optique, Université Paris Saclay, Palaiseau 91127 Cedex, France*

Martin Wegener − *Institute of Applied Physics, Karlsruhe Institute of Technology, Karlsruhe 76131, Germany; Institute of Nanotechnology, Karlsruhe Institute of Technology, Karlsruhe 76131, Germany*

Carsten Rockstuhl − *Institute of Nanotechnology, Karlsruhe Institute of Technology, Karlsruhe 76131, Germany; Institute of Theoretical Solid State Physics, Karlsruhe Institute of Technology, Karlsruhe 76131, Germany*

Andriy Shevchenko − *Department of Applied Physics, Aalto University, Aalto FI-00076, Finland*

Complete contact information is available at:
https://pubs.acs.org/10.1021/acsphotonics.6c01233

Funding

P.H. and A.S. acknowledge funding from the Research Council of Finland Flagship Programme, Photonics Research and Innovation (PREIN), decision number 346529. S.K. and M.W. acknowledge funding by the Deutsche Forschungsgemeinschaft (DFG, German Research Foundation) under Germany's Excellence Strategy for the Excellence Cluster "3D Matter Made to Order" (2082/1 and 2082/2-390761711), by the Carl Zeiss Foundation, and by the Helmholtz program Materials Systems Engineering. M.N. acknowledges support by the KIT through the Virtual Materials Design (Virtmat) project. S.H. acknowledges support from the Erasmus + mobility program.

Notes

The authors declare no competing financial interest.

REFERENCES

(1) Sibarita, J.-B. Advances in Biochemical Engineering. In *Deconvolution Microscopy*; Rietdorf, J., Ed.; Springer, 2005.

(2) Sage, D.; Donati, L.; Soulez, F.; Fortun, D.; Schmit, G.; Seitz, A.; Guiet, R.; Vonesch, C.; Unser, M. DeconvolutionLab2: An Open-Source Software for Deconvolution Microscopy. *Methods* **2017**, *115*, 28−41.

(3) McCann, M. T.; Jin, K. H.; Unser, M. Convolutional Neural Networks for Inverse Problems in Imaging: A Review. *IEEE Signal Process. Mag* **2017**, *34*, 85−95.

(4) Tian, C.; Fei, L.; Zheng, W.; Xu, Y.; Zuo, W.; Lin, C.-W. Deep Learning on Image Denoising: An Overview. *Neural Netw* **2020**, *131*, 251−275.

(5) Wali, A.; Naseer, A.; Tamoor, M.; Gilani, S. A. M. Recent Progress in Digital Image Restoration Techniques: A Review. *Digit. Signal Process* **2023**, *141*, 104187.

(6) Yanny, K.; Monakhova, K.; Shuai, R. W.; Waller, L. Deep Learning for Fast Spatially Varying Deconvolution. *Optica* **2022**, *9*, 96−99.

(7) Li, Y.; et al. Incorporating the Image Formation Process into Deep Learning Improves Network Performance. *Nat. Methods.* **2022**, *19*, 1427−1437.

(8) Banerjee, C.; Nguyen, K.; Fookes, C.; George, K. Physics-Informed Computer Vision: A Review and Perspectives. *ACM Comput. Surv.* **2025**, *57*, 1−38.

(9) Mezouari, S.; Harvey, A. R. Phase Pupil Functions for Reduction of Defocus and Spherical Aberrations. *Opt. Lett.* **2003**, *28*, 771−773.

(10) Zhao, H.; Li, Y. Performance of an Improved Logarithmic Phase Mask with Optimized Parameters in a Wavefront-Coding System. *Appl. Opt.* **2010**, *49*, 229−238.

(11) Le, V. N.; Fan, Z.; Minh, N. P.; Chen, S. Optimized Square-Root Phase Mask to Generate Defocus-Invariant Modulation Transfer Function in Hybrid Imaging Systems. *Opt. Eng.* **2015**, *54*, 035103.

(12) Astratov, V. N.; Sahel, Y. B.; Eldar, Y. C.; Huang, L.; Ozcan, A.; Zheludev, N.; Zhao, J.; Burns, Z.; Liu, Z.; Narimanov, E.; et al. Roadmap on Label-Free Super-Resolution Imaging. *Laser Photonics Rev.* **2023**, *17*, 2200029.

(13) Fish, D. A.; Brinicombe, A. M.; Pike, E. R.; Walker, J. G. Blind Deconvolution by Means of the Richardson−Lucy Algorithm. *J. Opt. Soc. Am. A* **1995**, *12*, 58−65.

(14) Chaudhuri, S.; Velmurugan, R.; Rameshan, R. *Blind Image Deconvolution*; Springer International Publishing, 2014; pp 37−60.

(15) Hegedus, Z. S. Annular Pupil Arrays. *Opt. Acta Int. J. Opt.* **1985**, *32*, 815−826.

(16) Ojeda-Castañeda, J.; Andrés, P.; Díaz, A. Annular Apodizers for Low Sensitivity to Defocus and to Spherical Aberration. *Opt. Lett.* **1986**, *11*, 487−489.

(17) Ojeda-Castañeda, J.; Berriel-Valdos, L. R.; Montes, E. Bessel Annular Apodizers: Imaging Characteristics. *Appl. Opt.* **1987**, *26*, 2770−2772.

(18) Hildén, P.; Shevchenko, A. Extended Depth of Field of an Imaging System with an Annular Aperture. *Opt. Express* **2023**, *31*, 11102−11115.

(19) Kolodziejczyk, A.; Bará, S.; Jaroszewicz, Z.; Sypek, M. The Light Sword Optical Element—a New Diffraction Structure with Extended Depth of Focus. *J. Mod. Opt.* **1990**, *37*, 1283−1286.

(20) Davidson, N.; Friesem, A. A.; Hasman, E. Holographic Axilens: High Resolution and Long Focal Depth. *Opt. Lett.* **1991**, *16*, 523−525.

(21) Zalvidea, D.; Sicre, E. E. Phase Pupil Functions for Focal-Depth Enhancement Derived from a Wigner Distribution Function. *Appl. Opt.* **1998**, *37*, 3623−3627.

(22) Chi, W.; George, N. Electronic Imaging Using a Logarithmic Asphere. *Opt. Lett.* **2001**, *26*, 875−877.
(23) Sherif, S. S.; Jr, E. R. D.; Jr, W. T. C. Logarithmic Phase Filter to Extend the Depth of Field of Incoherent Hybrid Imaging Systems. *Proc. SPIE 4471, Algorithms and Systems for Optical Information Processing V* **2001**, 272−280.
(24) Ben-Eliezer, E.; Zalevsky, Z.; Marom, E.; Konforti, N. All-Optical Extended Depth of Field Imaging System. *J. Opt. A: Pure Appl. Opt.* **2003**, *5*, 164−169.
(25) Zhou, F.; Ye, R.; Li, G.; Zhang, H.; Wang, D. Optimized Circularly Symmetric Phase Mask to Extend the Depth of Focus. *J. Opt. Soc. Am. A* **2009**, *26*, 1889−1895.
(26) Sturges, T. J.; Nyman, M.; Kalt, S.; Pälsi, K.; Hilden, P.; Wegener, M.; Rockstuhl, C.; Shevchenko, A. Inverse-Designed 3D Laser Nanoprinted Phase Masks to Extend the Depth of Field of Imaging Systems. *ACS Photonics* **2024**, *11*, 3765−3773.
(27) Padgett, M. J.; Boyd, R. W. An Introduction to Ghost Imaging: Quantum and Classical. *Philos. Trans. R. Soc. A* **2017**, *375*, 20160233.
(28) Ilina, E.; Nyman, M.; Švagždytė, I.; Chekurov, N.; Kaivola, M.; Setälä, T.; Shevchenko, A. Aberration-Insensitive Microscopy Using Optical Field-Correlation Imaging. *APL Photonics* **2019**, *4*, 066102.
(29) Ilina, E.; Nyman, M.; Mondal, T.; Kaivola, M.; Setälä, T.; Shevchenko, A. Interferometric Imaging of Reflective Micro-Objects in the Presence of Strong Aberrations. *Opt. Express* **2020**, *28*, 1817−1826.
(30) Hannonen, A.; Shevchenko, A.; Friberg, A.; Setälä, T. Temporal Phase-Contrast Ghost Imaging. *Phys. Rev. A* **2020**, *102*, 063524.
(31) Jiang, H.; Huang, G.; Wilford, P. Multi-View in Lensless Compressive Imaging. *APSIPA Trans. Signal Inf. Process.* **2014**, *3*, No. e15.
(32) Edgar, M. P.; Gibson, G. M.; Padgett, M. J. Principles and Prospects for Single-Pixel Imaging. *Nat. Photonics* **2019**, *13*, 13−20.
(33) Dowski, E. R.; Cathey, W. T. Extended Depth of Field through Wave-Front Coding. *Appl. Opt.* **1995**, *34*, 1859−1866.
(34) Chu, K.; George, N.; Chi, W. Extending the Depth of Field through Unbalanced Optical Path Difference. *Appl. Opt.* **2008**, *47*, 6895−6903.
(35) Mo, X. Optimized Annular Phase Masks to Extend Depth of Field. *Opt. Lett.* **2012**, *37*, 1808−1810.
(36) Lopez-Ramirez, M.; Ledesma-Carrillo, L. M.; Cabal-Yepez, E.; Botella, G.; Rodriguez-Donate, C.; Ledesma, S. FPGA-based Methodology for Depth-of-Field Extension in a Single Image. *Digit. Signal Process.* **2017**, *70*, 14−23.
(37) Atalay Appak, I. A.; Sahin, E.; Guillemot, C.; Caglayan, H. Learning Flat Optics for Extended Depth of Field Microscopy Imaging. *Nanophotonics* **2023**, *12*, 3623−3632.
(38) Zhao, H.; Li, Y. Optimized Sinusoidal Phase Mask to Extend the Depth of Field of an Incoherent Imaging System. *Opt. Lett.* **2010**, *35*, 267−269.
(39) Muyo, G.; Harvey, A. R. Decomposition of the Optical Transfer Function: Wavefront Coding Imaging Systems. *Opt. Lett.* **2005**, *30*, 2715−2717.
(40) Demenikov, M.; Harvey, A. R. Image Artifacts in Hybrid Imaging Systems with a Cubic Phase Mask. *Opt. Express* **2010**, *18*, 8207−8212.
(41) Barwick, D. S. Increasing the Information Acquisition Volume in Iris Recognition Systems. *Appl. Opt.* **2008**, *47*, 4684−4691.
(42) Sherif, S. S.; Cathey, W. T.; Dowski, E. R. Phase Plate to Extend the Depth of Field of Incoherent Hybrid Imaging Systems. *Appl. Opt.* **2004**, *43*, 2709−2721.
(43) Li, Z.; Hou, Q.; Wang, Z.; Tan, F.; Liu, J.; Zhang, W. End-to-End Learned Single Lens Design Using Fast Differentiable Ray Tracing. *Opt. Lett.* **2021**, *46*, 5453−5456.
(44) Sun, Q.; Wang, C.; Fu, Q.; Dun, X.; Heidrich, W. End-to-End Complex Lens Design with Differentiate Ray Tracing. *ACM Trans. Graph.* **2021**, *40*, 1−13.
(45) Sitzmann, V.; Diamond, S.; Peng, Y.; Dun, X.; Boyd, S.; Heidrich, W.; Heide, F.; Wetzstein, G. End-to-End Optimization of Optics and Image Processing for Achromatic Extended Depth of Field and Super-Resolution Imaging. *ACM Trans. Graph.* **2018**, *37* (114), 1−114.
(46) Fontbonne, A.; Sauer, H.; Goudail, F. End-to-End Optimization of Optical Systems with Extended Depth of Field under Wide Spectrum Illumination. *Appl. Opt.* **2022**, *61*, 5358−5367.
(47) Zhang, R.; Tan, F.; Hou, Q.; Li, Z.; Sun, Z.; Yang, C.; Gao, X. End-to-End Learned Single Lens Design Using Improved Wiener Deconvolution. *Opt. Lett.* **2023**, *48*, 522−525.
(48) Oliva, E.; Díaz, N.; Pinilla, S.; Vera, E. Multispectral Extended Depth-of-Field Imaging via Stochastic Wavefront Optimization. *IEEE Open J. Signal Process* **2025**, *6*, 965−974.
(49) Carles, G.; Carnicer, A.; Bosch, S. Phase Mask Selection in Wavefront Coding Systems: A Design Approach. *Opt. Lasers Eng.* **2010**, *48*, 779−785.
(50) Demenikov, M. Development of Compact Optical Zoom Lenses with Extended-Depth-of-Field. *Proc. SPIE 8488, Zoom Lenses* **2012**, *IV*, 130−145.
(51) Richardson, W. H. Bayesian-Based Iterative Method of Image Restoration. *J. Opt. Soc. Am.* **1972**, *62*, 55−59.
(52) Lucy, L. B. An Iterative Technique for the Rectification of Observed Distributions. *Astron. J.* **1974**, *79*, 745.
(53) Guo, M.; et al. Rapid Image Deconvolution and Multiview Fusion for Optical Microscopy. *Nat. Biotechnol.* **2020**, *38*, 1337−1346.
(54) Goodman, J. W. *Introduction to Fourier Optics*; Roberts & company, 2005.
(55) Van Haver, S.; Janssen, A. J. E. M. Advanced Analytic Treatment and Efficient Computation of the Diffraction Integrals in the Extended Nijboer-Zernike Theory. *J. Eur. Opt. Soc., Rapid publ.* **2013**, *8*, 13044.
(56) Born, M.; Wolf, E. *Principles of Optics: Electromagnetic Theory of Propagation, Interference and Diffraction of Light*; Elsevier Science & Technology, 1980.
(57) Rao, A. S. A Conceptual Review on Bessel Beams. *Phys. Scr.* **2024**, *99*, 062007.
(58) Pitman, J. *Probability*; Springer: New York, 1993.
(59) Kabuli, L. A.; Pinkard, H.; Markley, E.; Hung, C. S.; Waller, L. Designing Lensless Imaging Systems to Maximize Information Capture. *Optica* **2026**, *13*, 227.
(60) Ng, M. K.; Chan, R. H.; Tang, W.-C. A Fast Algorithm for Deblurring Models with Neumann Boundary Conditions. *SIAM J. Sci. Comput* **1999**, *21*, 851−866.
(61) Liu, R.; Jia, J. Reducing Boundary Artifacts in Image Deconvolution. In *2008. 15th IEEE International Conference on Image Processing*; ICIP, 2008; pp 505−508.
(62) Wang, Z.; Bovik, A.; Sheikh, H.; Simoncelli, E. Image Quality Assessment: From Error Visibility to Structural Similarity. *IEEE Trans. Image Process.* **2004**, *13*, 600−612.
(63) Zhao, H.; Gallo, O.; Frosio, I.; Kautz, J. Loss Functions for Image Restoration With Neural Networks. *IEEE Trans. Comput. Imaging* **2017**, *3*, 47−57.
(64) Wang, H. ImageNet-Sketch. (available at: https://github.com/HaohanWang/ImageNet-Sketch) 2025; (Accessed Nov 20, 2025)
(65) Abadi, M. et al. TensorFlow, Large-scale Machine Learning on Heterogeneous Systems. (available at: https://github.com/tensorflow/tensorflow) 2015; (Accessed Nov 26, 2025)
(66) Kingma, D. P.; Ba, J. Adam: A Method for Stochastic Optimization. *arXiv* **2017**, 1412.6980.
(67) Weinacker, J.; Kalt, S.; Kiefer, P.; Rietz, P.; Wegener, M. On Iterative Pre-Compensation of 3D Laser-Printed Micro-Optical Components Using Confocal-Optical Microscopy. *Adv. Funct. Mater.* **2024**, *34*, 2309356.
(68) Schmid, M.; Ludescher, D.; Giessen, H. Optical Properties of Photoresists for Femtosecond 3D Printing: Refractive Index, Extinction, Luminescence-Dose Dependence, Aging, Heat Treatment and Comparison between 1-Photon and 2-Photon Exposure. *Opt. Mater. Express* **2019**, *9*, 4564−4577.

https://doi.org/10.1021/acsphotonics.6c01233
ACS Photonics XXXX, XXX, XXX−XXX